Cilt 11, Sayı 3, Sayfa 44-50, 2022 Volume 11, Issue 3, Page 44-50, 2022

Araştırma Makalesi https://doi.org/10.46810/tdfd.1094576 Research Article

Türk Doğa ve Fen Dergisi
Turkish Journal of Nature and Science
www.dergipark.gov.tr/tdfd

Thermal Conductivity and Thermal Rectification in Various Sequences of Monolayer Hexagonal Boron Nitride/Aluminum Nitride Superlattice Nanoribbons

Yenal KARAASLAN[1,2*]

[1]Department of Fundamental Sciences, Air NCO Vocational HE School, Turkish National Defence University, 35415 İzmir, Türkiye
[2]Department of Mechanical Engineering, Eskisehir Technical University, 26555 Eskişehir, Türkiye
Yenal KARAASLAN ORCID No: 0000-0001-8483-4819

**Corresponding author: ykaraaslan@msu.edu.tr, yenalkaraaslan@gmail.com*

(Received: 28.03.2022, Accepted: 29.07.2022, Online Publication: 29.09.2022)

Keywords
Thermal conductivity, Thermal rectification, Monolayer BN/AlN superlattice nanoribbons

Abstract: In this study, the thermal transport properties for various geometries of monolayer *h*-BN/*h*-AlN superlattice nanoribbons are investigated using non-equilibrium molecular dynamics simulations. In this context, the lattice thermal conductivities of the superlattice nanoribbons are obtained for different period lengths, geometries, sample lengths, and temperatures. Results reveal that a decrease in the thermal conductivities of superlattice nanoribbons when compared with those of the pristine nanoribbons, the lattice thermal conductivities decrease with decreasing sample lengths and increasing temperatures, also the formation of the extremum points resulting from the competition between wave-like and particle-like phonon transport in the thermal conductivity of superlattice nanoribbons with the change of the period lengths. Moreover, superlattice nanoribbons with different geometries are created to connect the *h*-BN/*h*-AlN interface, and it is observed that there is a difference between the thermal conductivities calculated in the reverse directions. This difference leads to thermal rectification in the superlattice structures. As the asymmetry between thermal contact areas increases especially at low temperatures, it is found out the thermal rectification ratio increases.

Tek Katmanlı Hegzagonal Bor Nitrür/Alüminyum Nitrür Süperörgü Nanoşeritlerinin Çeşitli Dizilerinde Termal İletkenlik ve Termal Doğrultma

Anahtar Kelimeler
Termal iletkenlik, Termal doğrultma, Tek katmanlı BN/AlN süperörgü nanoşeritler

Öz: Bu çalışmada, tek-katmanlı h-BN/h-AlN süperörgü nanoşeritlerinin çeşitli geometrileri için termal taşınım özellikleri, denge dışı moleküler dinamik simülasyonları kullanılarak araştırılmıştır. Bu bağlamda, farklı periyot uzunlukları, geometriler, örnek uzunlukları ve sıcaklıklar için süperörgü nanoşeritlerin örgü ısıl iletkenlikleri elde edilmiştir. Sonuçlar, bozulmamış nanoşeritler ile karşılaştırıldığında süperörgü nanoşeritlerin termal iletkenliklerinde bir azalma olduğunu, kafes termal iletkenliklerinin azalan örnek uzunlukları ve artan sıcaklıklar ile azaldığını, ayrıca periyot uzunluklarının değişimi ile süperörgü nanoşeritlerinin termal iletkenliklerinde dalga-benzeri ve parçacık-benzeri fonon taşınımı arasındaki rekabetten kaynaklanan ekstremum noktalarının oluşumunu ortaya koymaktadır. Ayrıca h-BN/h-AlN arayüzünü bağlamak için farklı geometrilere sahip süperörgü nanoşeritler yaratılmıştır ve ters yönlerde hesaplanan termal iletkenlikler arasında fark olduğu gözlemlenmektedir. Bu fark, süperörgü yapılarında termal doğrultmaya sebep olmaktadır. Özellikle düşük sıcaklıklarda termal banyo alanları arasındaki asimetri arttıkça termal doğrultma oranının arttığı tespit edilmiştir.

1. INTRODUCTION

Bulk group III-nitride semiconductor materials (BN, AlN, GaN, and InN) and their alloys have attracted great attention due to different device applications in electronics and optoelectronics as well as in thermoelectrics such as the high electron mobility transistors, laser diodes, light-emitting diodes, photo-detectors, solar cells, electro-optic modulators, and biosensors [1-4]. Nowadays, with the advance of fabrication technologies [5], interest in the hexagonal group-III nitride monolayers which possess graphene-like planar honeycomb structures have increased due to

both their potential in producing alternative solutions to graphene without band-gap (a disadvantage for thermoelectric applications) and their potential to achieve the desired device performances (high computing performance, low power consumption, etc.) for next-generation device applications [6,7]. Recently, the low-dimensional structures of BN [8,9], and AlN [10,11] have been successfully synthesized with high dimensional accuracy. Another class of low-dimensional nanomaterials is quasi-one-dimensional nanoribbons. The nanoribbons can be produced with techniques such as unwrapping of nanotubes [12] or cutting the monolayers, and so the phonons confined in bring novel properties to materials [13,14].

Controlling heat flow provides potential advantages in promising application fields such as thermoelectrics [15,16], thermal management [17,18], information processing [19], and optoelectronics [20]. In particular, the phonon interface scattering in structures such as two-dimensional superlattices is proposed as an alternative option in heat management applications. A superlattice implies a periodic or quasi-periodic arrangement of a certain period length layers composed of two or more crystal structures. In numerous experimental [21-23] and theoretical [24-26] studies, it has been pointed out that a superlattice with various components may indicate quite different thermal transport properties from the ones of its constituents due to due to its new translational symmetry and its capability to produce unusual phenomena [27-29]. Since the phonon mean-free-path is significantly suppressed by the phonon-boundary scattering at the interfaces between the materials, the lower lattice thermal conductivity of these structures compared to their constituents has been predicted [28-30].

One of the most fundamental phenomena associated with thermal manipulation in solid-state device applications is thermal rectification. The thermal rectification arises heterostructures (such superlattices) [31,32] or thermal asymmetry in the heat flow direction of asymmetric structures [33,34] or materials with asymmetric thermal contact [35,36]. For instance, by Chang et al. [37], heavy molecules were externally and in-homogeneously loaded to carbon and BN nanotubes, and about 7% thermal rectification coefficient was experimentally measured between the forward and backward directions by yielding asymmetric axial thermal conductance. In various asymmetric monolayer graphene nanostructures of the micrometer scale samples, the thermal rectification was experimentally measured by Wang et al. [34], and a 10% (26%) thermal rectification factor was reported for pristine monolayer graphene with nanoparticles deposited on one side or with a tapered width (for asymmetric monolayer graphene with nanopores on one side). Moreover, by Duan et al. [38], the interfacial thermal resistance between the carbon nanotube films and copper was experimentally measured, and the thermal rectification coefficient ranges between $57-68\%$ were presented. Also, the thermal rectification coefficient originated from phonon confinement in the lateral dimension in asymmetric T-shaped or trapezoidal graphene nanoribbons using molecular dynamics simulations was predicted around 10% by Wang et al. [39]. Lastly, the thermal rectification coefficient for nozzle-like graphene/boron nitride nanoribbons having various geometries has been estimated at values of up to 25% by Dehaghani et al. [40].

Consequently, knowing and understanding the thermal transport properties of materials by controlling the heat flow is important and necessary for promising next-generation thermal device applications. Therefore, investigation of the thermal behavior of heat carrier phonons in monolayer superlattice nanoribbons is chosen as the subject of this study for both to clearly understand its nature and to indicate can be used as a thermal management tool in low-dimensional layered systems. Here, the thermal transport properties of monolayer hexagonal BN/AlN (*h*-BN/*h*-AlN) superlattice nanoribbons using the non-equilibrium molecular dynamics (NEMD) simulations via the Large-scale Atomic/Molecular Massively Parallel Simulator (LAMMPS) [41,42] are investigated. To this end, the force-field Tersoff potential parameters reported previously are used to model inter-atomic interactions of the *h*-BN/*h*-AlN nanoribbons [43,44].

2. MATERIAL AND METHOD

Schematic representations of monolayer *h*-BN/*h*-AlN superlattice nanoribbons, Boron (B): blue circle, Aluminum (Al): green circle, Nitrogen (N): grey circle) are shown in Fig. 1. Periodic boundary conditions are applied in the *x*-direction where the heat flow direction, while free boundary conditions are put into practice in the *y*-direction. The L_y width is $16a$ ($a = 0.306$ nm is the lattice constant). For L_x eight different length values in the range of $120-768$ unit cells ($\sqrt{3}a$) are considered. Simulation cells that the numbers of atoms in materials to be the same are created for six different period lengths ($l_p = l_1, 2l_1, 3l_1, 4l_1, 6l_1, 12l_1$, where $l_1 = 1.060$ nm is the minimum period length). In addition, the simulation cells of nanoribbons, half of which is *h*-BN and the other half which of *h*-AlN, are created to connect the *h*-BN and *h*-AlN interface at four different angles ($\theta = 0^o, 30^o, 60^o,$ and 90^o). The NEMD simulations are performed for 7.5 ns with 0.5 fs time steps. Before applying the thermal gradient, the system is allowed to reach equilibrium at the desired temperature in the NVT ensemble for 1 ns. The thermal conductivity values are provided by using the data collected over the last 5 ns.

The thermal conductivity values of the superlattice nanoribbon simulation cells are obtained via Fourier's law

$$\kappa = -\frac{J}{\partial T/\partial x} \qquad (1)$$

by defining the heat flow, $J = \Delta Q/2A\Delta t$, removed from (or added to) the hot region (cold region) [45]. Here, $\partial T/\partial x$ is the temperature gradient generated between hot and cold regions along the heat flow direction, ΔQ is

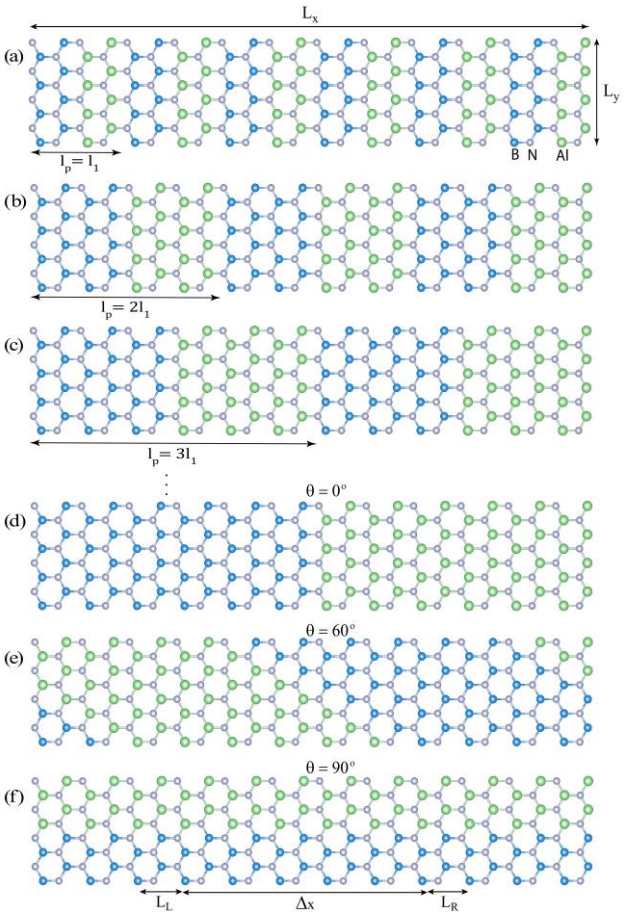

Figure 1. Some of the schematic representation of the monolayer h-BN/h-AlN superlattice nanoribbon sequences (a) $l_p = l_1$, (b) $l_p = 2l_1$, (c) $l_p = 3\,l_1$, (d) $l_p = L_x$ and $\theta = 0^o$, (e) $l_p = L_x$ and $\theta = 60^o$, and (f) $l_p = L_x$ and $\theta = 90^o$. Boron (B): blue circle, Aluminum (Al): green circle, Nitrogen (N): grey circle. Illustrative representation of thermal contacts (L_L and L_R) and sample geometry (width of L_y, length of L_x, symmetrical Δx length between contacts) in the MD simulations.

energy flux, Δt is the simulation time and A is the cross-sectional area that the heat flux passes through along simulation cells. The A is calculated considering l_z = 0.337 nm as the effective layer thickness of the monolayer nanoribbons [43]. Langevin thermostat that a stochastic heat bath [46], is used to establish thermal reservoirs in order to control the temperature difference as 60 K. The length of both hot and cold thermal reservoir regions (L_L and L_R, see Fig. 1) is kept constant as 16 unit cells $(16\sqrt{3}a)$ to form symmetrical thermal contacts.

The intrinsic lattice thermal conductivity of infinitely long samples is predicted through extrapolation of the finite sample length results determined from the NEMD simulations via [47]:

$$\frac{1}{\kappa(\Delta x)} = \frac{1}{\kappa_\infty}\left(\frac{l_{pmfp}}{\Delta x} + 1\right) \qquad (2)$$

here Δx (see Fig. 1) is the sample length between hot and cold reservoir regions, l_{pmfp} is the phonon mean-free-path, κ(Δx) is the thermal conductivity value obtained for the selected Δx length, and κ_∞ is the intrinsic lattice thermal conductivity of the real system with infinite length.

By exchanging the thermal asymmetry, the thermal rectification (TR) is calculated as:

$$TR(\%) = \frac{|\kappa^+ - \kappa^-|}{\kappa^-} \times 100 \qquad (3)$$

where κ^+ is the thermal conductivity while L_L: hot region and L_R: cold region, and κ^- is for the reverse.

3. RESULTS

Intrinsic lattice thermal conductivity of the monolayer *h*-BN/*h*-AlN superlattice nanoribbons is estimated using the extrapolation function in Eq. 2 over the thermal conductivities calculated for the simulations of the finite sample lengths along the *x*-direction. In Fig. 2(a)- (c), the extrapolated data for six different superlattice period lengths of the superlattice nanoribbons are given at 200 K, 300 K, and 600 K temperatures, respectively. In the thermal conductivity results of six different superlattice period lengths, eight different finite simulation sample lengths are taken into account for extrapolations, and only a single NEMD simulation is carried out to determine the thermal conductivities of the finite sample lengths. The increment in nanoribbon sample length contributes to the thermal conduction as brings about an increase in the total phonon life-times along the heat flux direction, and thus the lattice thermal conductivities increase with increasing ribbon length.

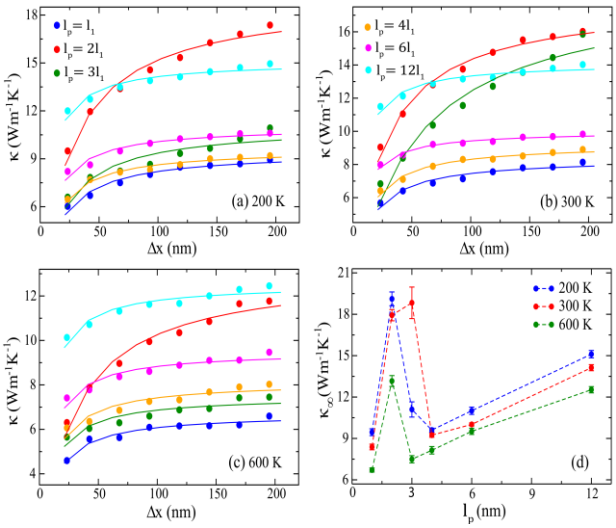

Figure 2. Period length dependent lattice thermal conductivity as a function of the Δx length for the monolayer h-BN/h-AlN superlattice nanoribbons at (a) 200 K, (b) 300 K, and (c) 600 K. Here, the line fit curves drawn in the same color as the data of each period length are generated using Eq. 2. (d) Intrinsic lattice thermal conductivity as a function of the period length at 200, 300, and 600 K temperatures for the monolayer h-BN/h-AlN superlattice nanoribbons.

Fig. 2(d) show the estimated intrinsic lattice thermal conductivity values of the monolayer *h*-BN/*h*-AlN superlattice nanoribbons as a function of superlattice period lengths at 200 K, 300 K, and 600 K. The standard deviations are determined from the fit curve of the thermal conductivity data obtained for the

simulations with finite sample lengths, using the function in Eq. 2. The intrinsic thermal conductivities of the superlattice nanoribbons at all the period lengths decrease with increasing temperatures as expected, due to the enhancement of the Umklapp process domination [27,48]. When compared with those of the pristine nanoribbon structures given in Table 1, the reduction in the thermal conductivities of superlattice nanoribbons is observed. Note that, the intrinsic lattice thermal conductivities of the monolayer *h*-BN and *h*-AlN pristine nanoribbons given in Table 1 have been calculated by using the same NEMD procedure for comparability [49].

Table 1. Intrinsic lattice thermal conductivity of pristine monolayer *h*-BN, and *h*-AlN nanoribbons obtained using the NEMD simulations at 200, 300, and 600 K temperatures [49].

κ_∞/Temperature	200 K	300 K	600 K
h-BN ($Wm^{-1}K^{-1}$)	337.79 ± 3.58	231.46 ± 2.44	122.51 ± 1.60
h-AlN ($Wm^{-1}K^{-1}$)	76.31 ± 0.58	54.66 ± 0.52	30.25 ± 0.63

A remarkable characteristic in the thermal conductivity of superlattice nanoribbons for all temperatures in Fig. 2(d) is the observation of extremum points with the change of the period length of superlattice nanoribbons. This extremum thermal conductivity behavior of the superlattice nanoribbons for the specific superlattice period lengths is consistent with previous results of studies both theoretically [25,26] and experimentally [22,50] performed for bulk and besides low-dimensional [27-30] superlattice structures. The increment of thermal conductivity in different superlattice period lengths implies the incoherent phonon transport where particle-like properties are dominant, while the decrement of thermal conductivity in different superlattice period lengths implies the coherent phonon transport in which wave-like properties are dominant [23].

Fig. 3 presents the temperature profiles of the NEMD simulations belonging to six different period lengths for *h*-BN/*h*-AlN superlattice nanoribbons with $L_x = 288$ unit cells at 300 K. The temperature profiles are smoother for shorter superlattice period lengths, and these imply that there is no resistance caused by local scattering, thus the superlattice nanoribbons can behave like a homogeneous structure. The jumping behavior in the temperature at the superlattice interfaces with increasing period lengths can comment as a series of thermal resistors for superlattice nanoribbons [29]. The behavior of the temperature profiles makes meaningful the interpretation of coherent and incoherent phonon transport for different superlattice period lengths.

In addition to superlattice nanoribbons with different period lengths, the superlattices of nanoribbons, half of which is *h*-BN and the other half which of *h*-AlN, are created to connect the *h*-BN and *h*-AlN interface at four different angles ($\theta = 0^o, 30^o, 60^o,$ and 90^o). Here, two different thermal conductivity values (κ^+, and κ^-) are calculated for the 0^o, 30^o, 60^o angles, considering that the energy flow from the hot region to the cold region may vary from the energy flow in the inverse

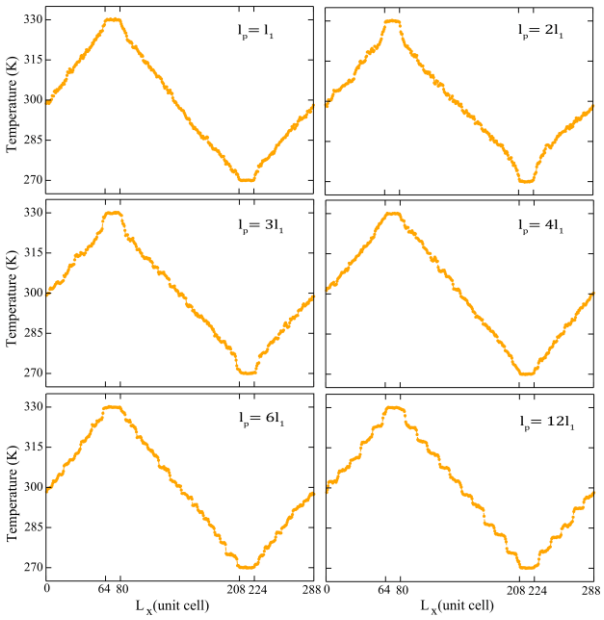

Figure 3. Temperature profiles of the monolayer h-BN/h-AlN superlattice nanoribbons with $L_x = 288$ unit cells for the period lengths $l_p = l_1,\ 2l_1,\ 3l_1,\ 4l_1,\ 6l_1,\ 12l_1$, at 300 K.

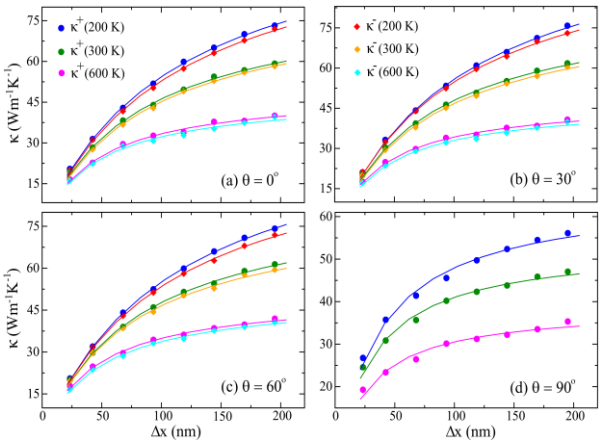

Figure 4. $\boldsymbol{\kappa^+}$ and $\boldsymbol{\kappa^-}$ lattice thermal conductivities of the monolayer h-BN/h-AlN superlattice nanoribbons as a function of the $\boldsymbol{\Delta x}$ length for $\boldsymbol{\theta}$ values of (a) $\mathbf{0^o}$, (b) $\mathbf{30^o}$, (c) $\mathbf{60^o}$, and (d) $\mathbf{90^o}$, at **200**, **300**, and **600** K temperatures. The line fit curves drawn in the same color as the data of each temperature are generated using Eq. 2.

case, due to the different atom arrangements at the superlattice interface for these structures. In Fig. 4, the thermal conductivity data determined according to Eq. 1 and extrapolation curves according to Eq. 2 based on these data are given as a function of the nanoribbon sample lengths for four different connect angles of the *h*-BN/*h*-AlN superlattice nanoribbon structures at 200 K, 300 K, and 600 K.

Table 2 demonstrates the intrinsic thermal conductivities and thermal rectification results of the monolayer *h*-BN/*h*-AlN superlattice nanoribbons for $\theta = 0^o$, 30^o, 60^o, and 90^o at 200, 300, and 600 K temperatures. Here, the discussed superlattices should not be considered as different from the superlattices created for the various period lengths discussed above. Because the superlattice created for the 0^o is actually a superlattice with $l_p = L_x$ period length. The 30^o and 60^o angles are superlattices developed to increase the asymmetry at the

interface. 90° offers a useful superlattice structure to manipulate thermal conductivity results in a different way. When the calculated thermal conductivity results are evaluated, it is observed that the results for the θ values of 0°, 30°, and 60° at all temperatures are close to each other, but the results for the 90° are approximately 40% lower than the results of other angles. Determining different thermal conductivities in the reverse directions for $\theta = 0^o, 30^o,$ and 60^o can be attributed to the differences in phonon transmissivity caused by asymmetric structures. These differences lead to thermal rectification in the superlattice structures. As the rate of asymmetry between connect areas increases at 200 K, and 300 K, the rate of thermal rectification also increases. However, the thermal rectification ratio at 600 K, on the contrary, decreases with increasing angles.

Table 2. Intrinsic lattice thermal conductivity of the monolayer h-BN/h-AlN superlattice nanoribbons for $\theta = 0^o, 30^o, 60^o,$ *and* 90^o at 200, 300, and 600 K temperatures. Thermal rectification rates for the θ values of $0^o, 30^o,$ and 60^o at all temperatures.

Angle (°)	Temperature (K)	κ_∞^+ ($Wm^{-1}K^{-1}$)	κ_∞^- ($Wm^{-1}K^{-1}$)	TR (%)
0	200	116.79 ± 1.67	113.33 ± 2.00	3.05
	300	84.36 ± 1.37	83.99 ± 1.59	0.44
	600	49.30 ± 0.99	47.65 ± 1.18	3.46
30	200	117.81 ± 1.67	111.87 ± 1.50	5.31
	300	86.09 ± 1.20	84.10 ± 1.69	2.36
	600	48.32 ± 0.67	47.14 ± 0.91	2.51
60	200	117.55 ± 1.17	110.06 ± 1.04	6.80
	300	86.35 ± 1.33	82.64 ± 1.20	4.49
	600	50.62 ± 0.89	50.08 ± 0.82	1.08
90	200	65.39 ± 1.57	-	-
	300	53.40 ± 1.31	-	-
	600	38.70 ± 1.27	-	-

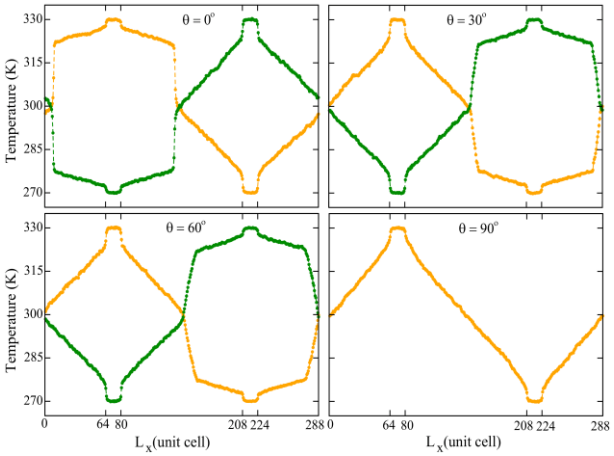

Figure 5. Temperature profiles of the monolayer h-BN/h-AlN superlattice nanoribbons with $L_x = 288$ unit cells for θ values of 0^o, 30^o, 60^o, and 90^o at 300 K. Orange curves for L_L: hot region and L_R: cold region, and green curves for the reverse.

The temperature profiles of the NEMD simulations for four different angles of *h*-BN/*h*-AlN superlattice nanoribbons with $L_x = 288$ unit cells are presented in Fig. 5. In the figures, the orange curves are the results of the simulations that take account of the energy flow from the hot region to the cold region, while the green curves are the results of the simulations that take into account the energy flow of the cold region to the hot region. For the 0°, 30°, and 60° angles, both materials are located in different temperature regions and therefore it is observed that the temperature profiles exhibit sharp transitions at the interface of the superlattices. While the transitions are sharper at lower angles, the transitions become smoother as the angle values increase. At the θ value of 90°, where the superlattice is like a homogeneous structure, a smooth temperature profile is displayed as expected.

The obtained results for the *h*-BN and *h*-AlN superlattice nanoribbons show up that the thermal conductivity of these structures can be controlled by superlattice sample length, temperature, and various geometries. The temperature across the reservoir regions for device applications of materials with high thermal conductivity reaches equilibrium very quickly, and this renders the thermoelectric device useless. Therefore, materials with low thermal conductivity are needed for thermoelectric device applications. The reduction of lattice thermal conductivity by inhibiting phonon propagation is one of the best ways to reduce the thermal conductivity of materials. Results of this study can be interpreted as the *h*-BN and *h*-AlN superlattice nanoribbons may be considered as a convenient choice to control the heat flow in thermoelectric device applications.

4. DISCUSSION AND CONCLUSION

Consequently, the thermal transport properties of the monolayer *h*-BN/*h*-AlN superlattice nanoribbons are analyzed using non-equilibrium molecular dynamics simulations. The thermal conductivities of the superlattices are determined as a function of the different period lengths, geometries, sample lengths, and temperatures. The estimated lattice thermal conductivity values of the superlattice nanoribbons are much lower than those of pristine structures, as expected. The results expose the extremum points in the lattice thermal conductivity that implies wave-like and particle-like phonon transport by controlling the period length of the superlattice nanoribbons. Also, the thermal conductivity of superlattice nanoribbons can be reduced with both decreasing sample lengths and increasing temperature. Besides, the thermal conductivities of the superlattice nanoribbons with non-symmetric geometries have a heat flow difference due to asymmetry in the reverse directions. This difference leads to thermal rectification in the superlattice structures. Especially at low temperatures, it is found out the thermal rectification factor can be increased up to 7% by adjusting the connect geometries. As a conclusion, this study presents detailed information on the thermal transport properties of the monolayer *h*-BN and *h*-AlN superlattice nanoribbons which could be used to manipulate the heat flow in thermal management and thermoelectric device applications.

Acknowledgement

I would like to give thanks to The Scientific and Technological Research Council of Turkey (TUBITAK) 2218-National Postdoctoral Research Fellowship Program (Project No: 118C455) for the financial support. The numerical calculations reported in this paper were completely performed at TUBITAK ULAKBIM, High Performance and Grid Computing Center (TRUBA resources).

REFERENCES

[1] Taniyasu Y, Kasu M, Makimoto T. An aluminium nitride light-emitting diode with a wavelength 210 nanometers. Nature. 2006;441(7091):325-8.
[2] Mokkapati S, Jagadish C. III-V compound SC for optoelectronic devices. Materials Today. 2009;12(4):22-32.
[3] Lu N, Ferguson I. III-nitrides for energy production: photovoltaic and thermoelectric applications. Semiconductor Science and Technology. 2013;28(7):074023.
[4] Li X, Liu X. Group III nitride nanomaterials for biosensing. Nanoscale. 2017;9(22):7320-41.
[5] Ambacher O. Growth and applications of group III-nitrides. Journal of Physics D: Applied physics. 1998;31(20):2653.
[6] Lu H, Guo Y, Robertson J. Chemical trends of Schottky barrier behavior on monolayer hexagonal B, Al, and Ga nitrides. Journal of Applied Physics. 2016;120(6):065302.
[7] Huang Z, Lü TY, Wang HQ, Yang SW, Zheng JC. Electronic and thermoelectric properties of the group-III nitrides (BN, AlN and GaN) atomic sheets under biaxial strains. Computational Materials Science. 2017;130:232-41.
[8] Song L, Ci L, Lu H, Sorokin PB, Jin C, Ni J, et al. Large scale growth and characterization of atomic hexagonal boron nitride layers. Nano Letters. 2010;10(8):3209-15.
[9] Cheng TS, Summerfield A, Mellor CJ, Khlobystov AN, Eaves L, Foxon CT, et al. High-temperature molecular beam epitaxy of hexagonal boron nitride with high active nitrogen fluxes. Materials. 2018;11(7):1119.
[10] Tsipas P, Kassavetis S, Tsoutsou D, Xenogiannopoulou E, Golias E, Giamini S, et al. Evidence for graphite-like hexagonal AlN nanosheets epitaxially grown on single crystal Ag (111). Applied Physics Letters. 2013;103(25):251605.
[11] Mansurov V, Malin T, Galitsyn Y, Zhuravlev K. Graphene-like AlN layer formation on (111) Si surface by ammonia molecular beam epitaxy. Journal of Crystal Growth. 2015;428:93-7.
[12] Zeng H, Zhi C, Zhang Z, Wei X, Wang X, Guo W, et al. “White graphenes”: boron nitride nanoribbons via boron nitride nanotube unwrap ping. Nano Letters. 2010;10(12):5049-55.
[13] Barone V, Peralta JE. Magnetic boron nitride nanoribbons with tunable electronic properties. Nano Letters. 2008;8(8):2210-4.
[14] Tabarraei A. Thermal conductivity of monolayer hexagonal boron nitride nanoribbons. Computational Materials Science. 2015;108:66-71.
[15] Tian Z, Lee S, Chen G. Heat transfer in thermoelectric materials and devices. Journal of Heat Transfer. 2013;135(6).
[16] Ouyang Y, Zhang Z, Li D, Chen J, Zhang G. Emerging theory, materials, and screening methods: new opportunities for promoting thermoelectric performance. Annalen der Physik. 2019;531(4):1800437.
[17] Feng CP, Wan SS, Wu WC, Bai L, Bao RY, Liu ZY, et al. Electrically insulating, layer structured SiR/GNPs/BN thermal management materials with enhanced thermal conductivity and breakdown voltage. Composites Science and Technology. 2018;167:456-62.
[18] Zhang Z, Ouyang Y, Cheng Y, Chen J, Li N, Zhang G. Size-dependent phononic thermal transport in low-dimensional nanomaterials. Physics Reports. 2020.
[19] Li N, Ren J, Wang L, Zhang G, Hänggi P, Li B. Colloquium: Phononics: Manipulating heat flow with electronic analogs and beyond. Reviews of Modern Physics. 2012;84(3):1045.
[20] Tien C, Chen G. Challenges in microscale conductive and radiative heat transfer. Previews of Heat and Mass Transfer. 1995;2(21):97.
[21] Yao T. Thermal properties of AlAs/GaAs superlattices. Applied Physics Letters. 1987;51(22):1798-800.
[22] Ravichandran J, Yadav AK, Cheaito R, Rossen PB, Soukiassian A, Suresha S, et al. Crossover from incoherent to coherent phonon scattering in epitaxial oxide superlattices. Nature materials. 2014;13(2):168-72.
[23] Cheaito R, Polanco CA, Addamane S, Zhang J, Ghosh AW, Balakrishnan G, et al. Interplay between total thickness and period thickness in the phonon thermal conductivity of superlattices from the nanoscale to the microscale: Coherent versus incoherent phonon transport. Physical Review B. 2018 Feb;97:085306.
[24] Juntunen T, Vänskä O, Tittonen I. Anderson localization quenches thermal transport in aperiodic superlattices. Physical Review Letters. 2019;122(10):105901.
[25] Latour B, Volz S, Chalopin Y. Microscopic de scription of thermal-phonon coherence: From coherent transport to diffuse interface scattering in superlattices. Physical Review B. 2014 Jul;90:014307.
[26] Chowdhury PR, Reynolds C, Garrett A, Feng T, Adiga SP, Ruan X. Machine learning maximized Anderson localization of phonons in aperiodic superlattices. Nano Energy. 2020;69:104428.
[27] Wang X, Wang M, Hong Y, Wang Z, Zhang J. Coherent and incoherent phonon transport in a graphene and nitrogenated holey graphene superlattice. Physical Chemistry Chemical Physics. 2017;19(35):24240-8.
[28] Zhu T, Ertekin E. Phonon transport on two-dimensional graphene/boron nitride superlattices.

Physical Review B. 2014;90(19):195209.
[29] Chen XK, Xie ZX, Zhou WX, Tang LM, Chen KQ. Phonon wave interference in graphene and boron nitride superlattice. Applied Physics Letters. 2016;109(2):023101.
[30] Felix IM, Pereira LFC. Suppression of coherent thermal transport in quasiperiodic graphene-hBN superlattice ribbons. Carbon. 2020;160:335-41.
[31] Chen XK, Xie ZX, Zhang Y, Deng YX, Zou TH, Liu J, et al. Highly efficient thermal rectification in carbon/boron nitride heteronanotubes. Carbon. 2019;148:532-9.
[32] Pei QX, Zhang YW, Sha ZD, Shenoy VB. Carbon isotope doping induced interfacial thermal resistance and thermal rectification in graphene. Applied Physics Letters. 2012;100(10):101901.
[33] Song C, Li S, Bao H, Ju J. Design of thermal diodes using asymmetric thermal deformation of a Kirigami structure. Materials & Design. 2020:108734.
[34] Wang H, Hu S, Takahashi K, Zhang X, Takamatsu H, Chen J. Experimental study of thermal rectification in suspended monolayer graphene. Nature Communications. 2017;8(1):1-8.
[35] Jiang P, Hu S, Ouyang Y, Ren W, Yu C, Zhang Z, et al. Remarkable thermal rectification in pristine and symmetric monolayer graphene enabled by asymmetric thermal contact. Journal of Applied Physics. 2020;127(23):235101.
[36] Lu J, Zheng Z, Yao J, Gao W, Xiao Y, Zhang M, et al. An asymmetric contact-induced self-powered 2D In_2S_3 photodetector towards high-sensitivity and fast-response. Nanoscale. 2020;12(13):7196-205.
[37] Chang CW, Okawa D, Majumdar A, Zettl A. Solid-state thermal rectifier. Science. 2006;314(5802):1121-4.
[38] Duan Z, Liu D, Zhang G, Li Q, Liu C, Fan S. Interfacial thermal resistance and thermal rectification in carbon nanotube film-copper systems. Nanoscale. 2017;9(9):3133-9.
[39] Wang Y, Vallabhaneni A, Hu J, Qiu B, Chen YP, Ruan X. Phonon lateral confinement enables thermal rectification in asymmetric single-material nanostructures. Nano Letters. 2014;14(2):592-6.
[40] Zarghami Dehaghani M, Molaei F, Spitas C, Hamed Mashhadzadeh A. Thermal rectification in nozzle-like graphene/boron nitride nanoribbons: A molecular dynamics simulation. Computational Materials Science. 2022;207:111320.
[41] Plimpton S. Fast parallel algorithms for short-range molecular dynamics. J Computational Physics. 1995;117(1):1 19.
[42] LAMMPS;. http://lammps.sandia.gov.
[43] Karaaslan Y, Yapicioglu H, Sevik C. Assessment of the thermal transport properties of group- III nitrides: A classical molecular dynamics study with transferable Tersoff-type inter-atomic potentials. Physical Review Applied. 2020 Mar;13:034027.
[44] Karaaslan Y. Coherent and incoherent phonon thermal transport in group-III nitride monolayer superlattices with Tersoff type interatomic potential. Physica E: Low-dimensional Systems and Nanostructures. 2022;140:115176.
[45] Müller-Plathe F. A simple nonequilibrium molecular dynamics method for calculating the thermal conductivity. The Journal of Chemical Physics. 1997;106(14):6082-5.
[46] Li Z, Xiong S, Sievers C, Hu Y, Fan Z, Wei N, et al. Influence of thermostatting on nonequilibrium molecular dynamics simulations of heat conduction in solids. The Journal of Chemical Physics. 2019;151(23):234105.
[47] Schelling PK, Phillpot SR, Keblinski P. Comparison of atomic-level simulation methods for computing thermal conductivity. Physical Review B. 2002 Apr;65:144306.
[48] Chen P, Zhang Z, Duan X, Duan X. Chemical synthesis of two dimensional atomic crystals, heterostructures and superlattices. Chemical Society Reviews. 2018;47(9):3129-51.
[49] Karaaslan Y. Thermal transport properties of hexagonal monolayer group-III nitride nanoribbons. Physica B: Physics of Condensed Matter. 2022; 640:414022.
[50] Saha B, Koh YR, Comparan J, Sadasivam S, Schroeder JL, Garbrecht M, et al. Cross-plane thermal conductivity of (Ti,W)N/(Al,Sc)N metal/semiconductor superlattices. Physical Review B. 2016 Jan;93:045311.